

Supporting Information

Elucidating the formation and active state of Cu co-catalysts for photocatalytic hydrogen evolution

Jasmin S. Schubert, Leila Kalantari, Andreas Lechner, Ariane Giesriegl, Sreejith P. Nandan, Pablo Alaya, Shun Kashiwaya, Markus Sauer, Annette Foelske, Johanna Rosen, Peter Blaha, Alexey Cherevan and Dominik Eder**

List of Sections and Figures/Tables

- 1. Hydrogen evolution reaction (HER):** Figure S1 and Table S1
 - 1.1. Calcination time effect on the HER activity: Figure S2
 - 1.2. Long-term performance (stability): Figure S3
- 2. Thermal behavior of the composites:** Figure S4
- 3. SEM and further TEM of the samples for Cu quantification:** Figure S5 and S6
- 4. Raman:** Table S2
- 5. XRD:** Table S3 and Figure S7
- 6. Infrared spectroscopy (FT-IR):** Figure S8 and S9
- 7. XPS:** Figure S10 -S13 and Table S4
- 8. XPS and XRF:** Table S5 and Figure S14
- 9. DRS, Tauc plots, UPS and VB-XPS:** Figure S15 - S17, Table S6 and S7
- 10. DRS and XRF before and after washing of Cu(NO₃)₂/TiO₂:** Figure S18 and Table S8
- 11 Cu amount effect on the HER activity:** Figure S19 and Table S9
- 12. DFT calculations:** Figure S20, Table S10 and S11

1. Hydrogen evolution reaction (HER)

A typical H₂ evolution profile obtained with our flow reactor (**Figure S1a**) includes an “induction” period that is related to the fact the H₂ gas needs to fill the dead volume (e.g., reactor volume, tubing volume) to reach the detector (see **Figure S1b,c** for the experimental setup). The delay in H₂ increase (2-3 minutes after illumination start) thus corresponds to the first H₂ species reaching the detector cell. A stable evolution rate is typically reached after 40-60 minutes of illumination.

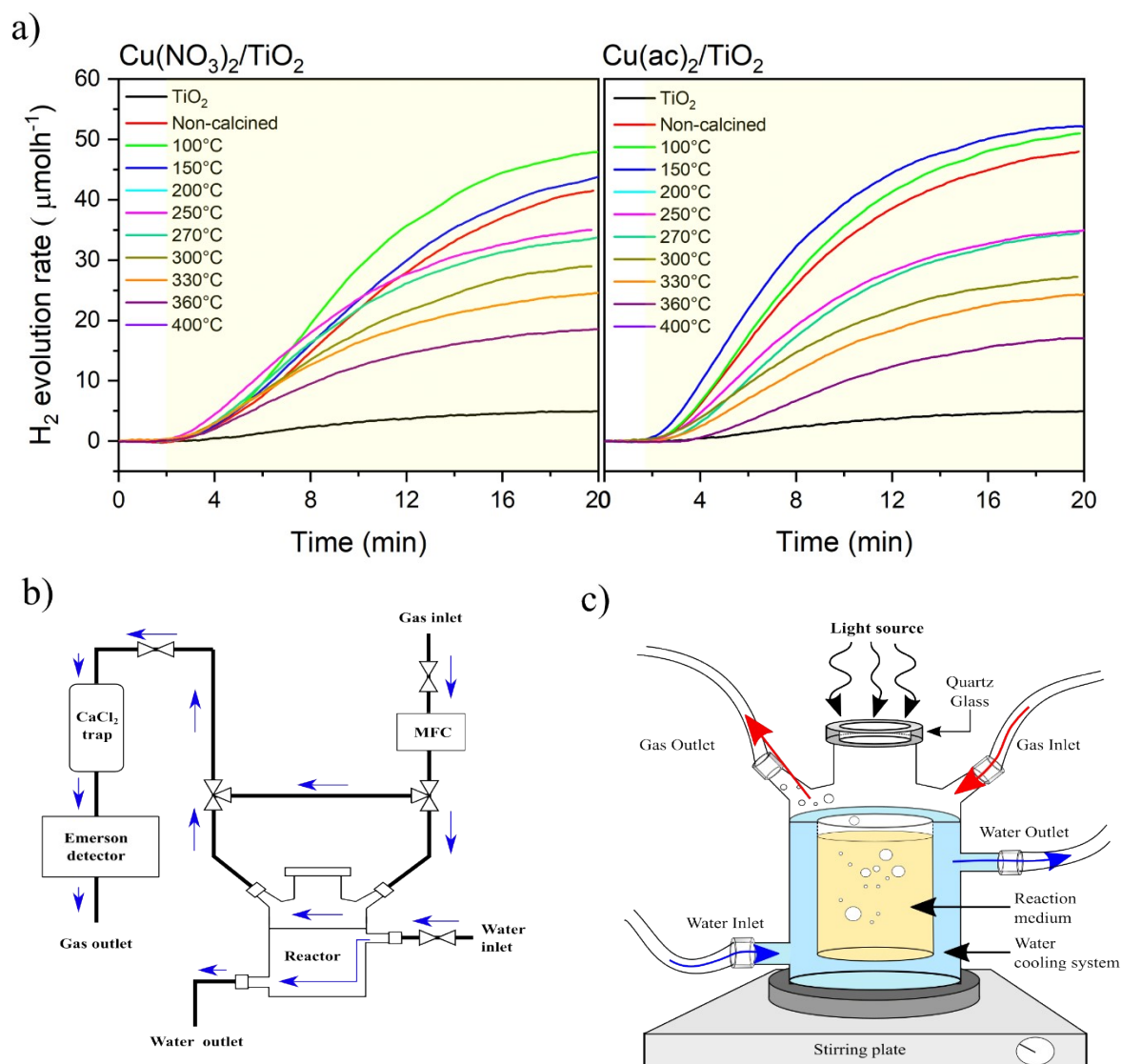


Figure S1: a) HER activity rates obtained for the different thermally treated Cu/TiO₂ composites along with the reference sample, TiO₂. The yellow region indicates the time of illumination. The bar graph, **Figure 1a**, in the main manuscript was constructed from these profiles at 20 minutes of illumination. b) Scheme of the photocatalytic setup used to evaluate HER rates (MFC: mass flow controller) and b) top-irradiation, flow-reactor used.

For this particular work, we were not interested in measuring the ultimate activities of the samples (e.g. waiting until the H₂ evolution rate reached a plateau), but - in order to speed up the photocatalytic evaluation - we only measured the activity value reached after 20 minutes of illumination (i.e. in the middle of the ascending slope). The values are reported in **Figure 1a** and allow for qualitative evaluation and comparison between the samples. The values are also representative of the absolute activity rates.

Table S1: HER rate maximum after 20 minutes of illumination. Values are taken from **Figure S1a** and represented in **Figure 1a**, in the main manuscript.

	H ₂ evolution rate, $\mu\text{mol h}^{-1}$	
	Cu(ac) ₂ /TiO ₂	Cu(NO ₃) ₂ /TiO ₂
TiO ₂	5.03	5.03
RT	47.97	41.47
100 °C	50.98	47.88
150 °C	52.18	43.55
200 °C	47.44	40.94
250 °C	37.88	35.01
270 °C	34.48	33.71
300 °C	27.22	28.98
330 °C	24.23	24.51
360 °C	17.29	18.55
400 °C	14.81	13.25

1.1. Calcination time effect on the HER activity

HER trend for the $\text{Cu}(\text{ac})_2/\text{TiO}_2$ sample hold from 44 to 655 minutes at 250 °C. This data shows that at constant temperature but longer calcination times, the activity decreases. Hence, this shows the same behavior than by increasing temperature but constant time. This data agrees with the hypothesis of doping, as longer calcination time would led to more time the system to equilibrate, i.e. Cu has more time to incorporate into the TiO_2 lattice. The amount of doping depends on the kinetics (time that it has to diffuse) and thermodynamics (temperature/energy).

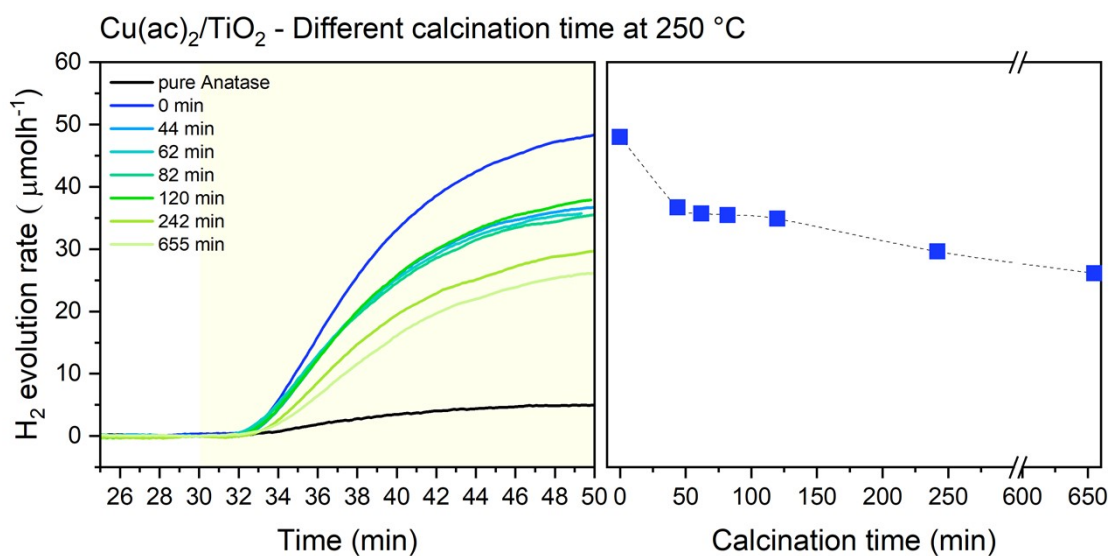


Figure S2. Time-dependend HER at a constant calcination temperature of 250 °C. a) HER vs reaction time. The yellow region is the illumination time. b) The HER at different calcination time after 20 minutes of illumination.

1.2. Long-term performance (stability)

With regard to the stability issue, long-term performance of our catalysts has been investigated using a combination of our flow-reactor and H₂ detection flow-cell by Emerson. **Figure S3** shows a 25 h HER run composed of two illumination cycles conducted for one of our Cu/TiO₂ samples. As clarified in the setup description, we observe a quick rise of “activity” that reaches a plateau within the first hour. Over the course of the next 17 h of illumination, H₂ evolution rate undergoes a slight but gradual drop (ca 18% of the max value) and reaches a new stability level. After the light is off (end of the first illumination cycle), we observe the expected drop of the H₂ evolution rate to zero. The second illumination cycle (the mutually compensating positive and negative spikes at 20 h point are related to carrier-gas supply change) yields activity similar to the second stability regime. Overall, these data illustrate a minor deactivation of the composite photocatalyst, however, they also indicate the overall stable long-term performance.

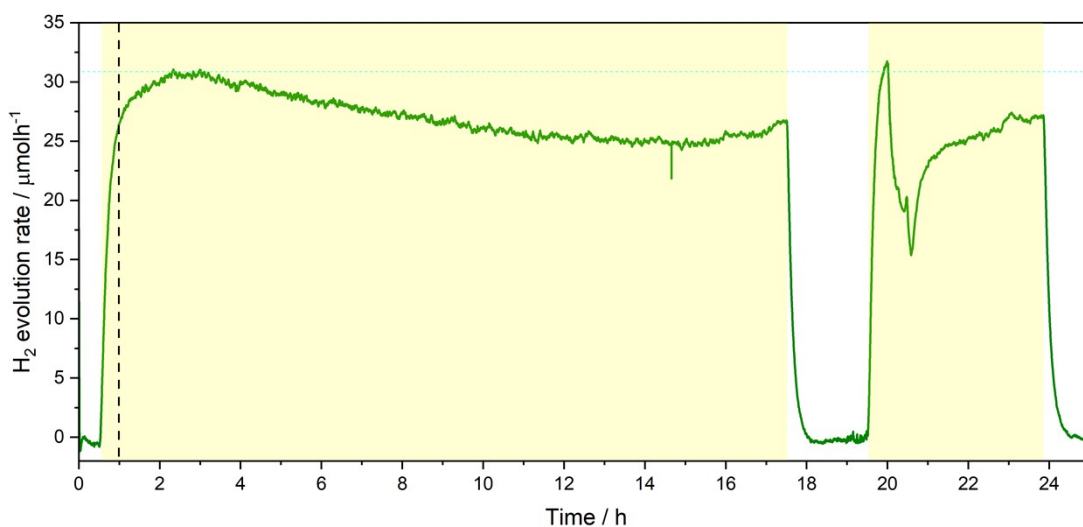


Figure S3. Long-term time-depended HER stability test of one of the Cu/TiO₂ samples.

2. Thermal behavior of the composites

We examined the pure precursors - $\text{Cu}(\text{ac})_2$ and $\text{Cu}(\text{NO}_3)_2$ – and the obtained composite $\text{Cu}(\text{ac})_2/\text{TiO}_2$ and $\text{Cu}(\text{NO}_3)_2/\text{TiO}_2$ powders with TGA (in air) to reveal the decomposition behavior. **Figure S4** shows the obtained weight loss profiles for the pure precursors, the composites and the reference TiO_2 powder. The continuous mass loss of the reference TiO_2 in the entire temperature range can be ascribed to slow removal of adsorbed (physisorbed and chemisorbed) solvent and other species; and, importantly, this reference profile can be treated as a baseline to quantitatively describe the behavior of composites. The analysis of the pure precursors shows that the first decomposition step starts at 82.3°C for both precursors and ending at 147.8°C for $\text{Cu}(\text{ac})_2$ and 179.9°C for $\text{Cu}(\text{NO}_3)_2$, corresponding to the evaporation of water molecules.^[1] The second step ranges from 251.5°C until 288.9°C for $\text{Cu}(\text{ac})_2$ and 213.2°C to 261.7°C for $\text{Cu}(\text{NO}_3)_2$. Corresponding to the decomposition of the acetate and nitrate ions, respectively. In the case of $\text{Cu}(\text{ac})_2$ the acetate ion undergoes decomposition via radical formation which leads to the formation of metallic Cu as an intermediate product before it gets re-oxidized at higher temperatures (see **Figure S4** from 288.9 to 800°C).^[2]

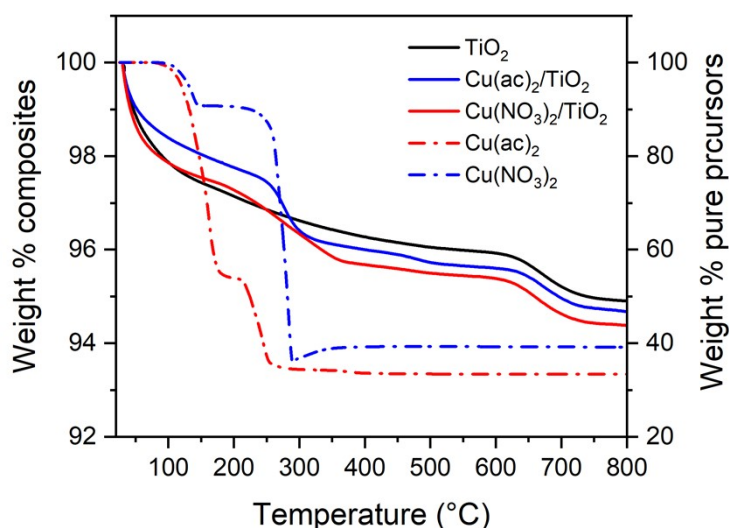


Figure S4: TGA data from 20°C to 800°C with a heating rate of 5°C min^{-1} of the reference TiO_2 , the pure precursors - $\text{Cu}(\text{ac})_2$ and $\text{Cu}(\text{NO}_3)_2$ – and the composites $\text{Cu}(\text{ac})_2/\text{TiO}_2$ and $\text{Cu}(\text{NO}_3)_2/\text{TiO}_2$. Note: The left y-axes correspond to the composites while the right y- axes to the pure precursors.

3. SEM and further TEM of the samples for Cu quantification

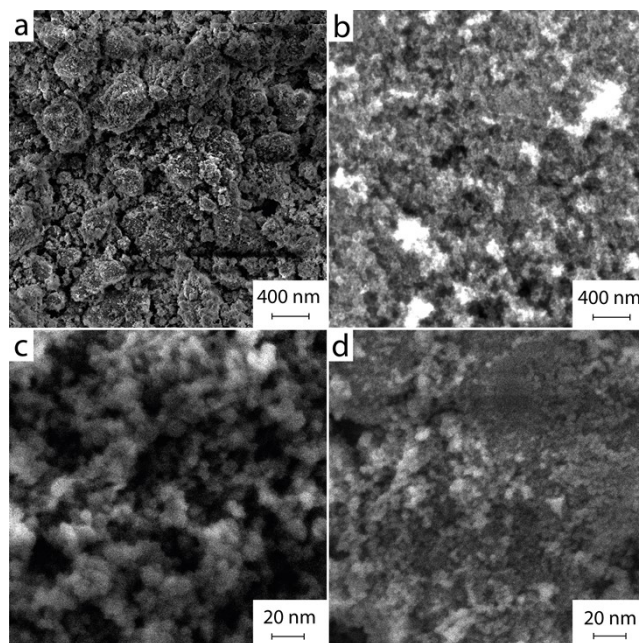


Figure S5: (a-d) SEM images of the as-prepared $\text{Cu}(\text{ac})_2/\text{TiO}_2$ composites.

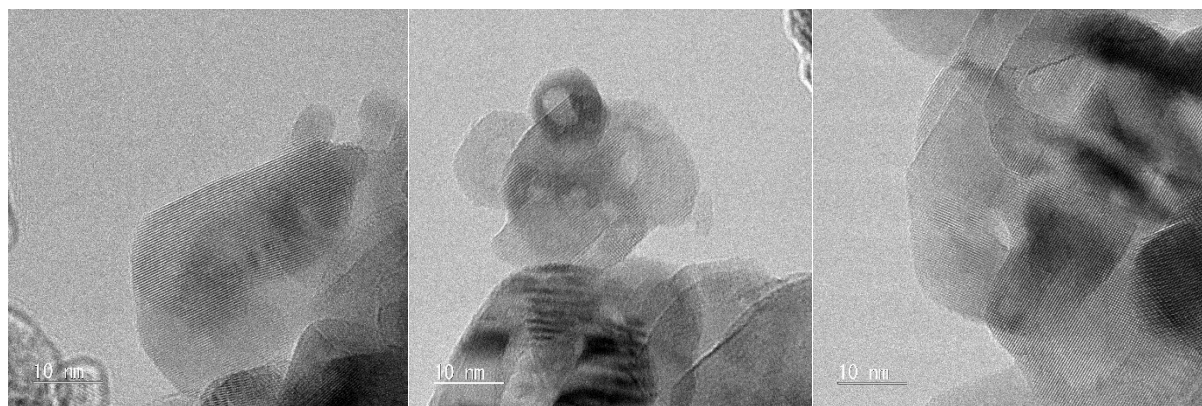


Figure S6: TEM pictures corresponding to $\text{Cu}(\text{ac})_2/\text{TiO}_2$ ranging from non-calcined to 400 °C (left to right).

4. Raman

Table S2. Raman peak positions, FWHM and Intensity maximum values. The FWHM error was obtained from the mathematical model used to determine the values from the raw data and was estimated to be $\pm 0.1 \text{ cm}^{-1}$ for both sample sets.

	Cu(ac) ₂ /TiO ₂			Cu(NO ₃) ₂ /TiO ₂		
	Peak position cm ⁻¹	FWHM cm ⁻¹	Intensity maximum a.u.	Peak position cm ⁻¹	FWHM cm ⁻¹	Intensity maximum a.u.
TiO ₂ -anatase	145.6	14.6	38825.7	146.3	14.5	46155.2
RT	146.1	15.5	26373.3	144.7	14.7	38156.0
100 °C	146.1	15.5	26908.0	145.3	14.7	36622.2
200 °C	146.1	15.1	25247.7	145.8	15.1	33309.5
250 °C	146.6	15.5	22275.3	146.3	15.2	27572.4
270 °C	146.6	15.2	21890.7	146.3	14.8	27534.5
330 °C	146.6	16.4	19226.7	146.8	15.4	21843.3
360 °C	146.1	15.9	17179.3	146.3	14.6	17432.8
400 °C	146.1	15.8	18781.0	146.8	15.2	21725.2

5. XRD

Pure precursor: In-situ XRD diffractograms were taken from the pure precursors, $\text{Cu}(\text{ac})_2$ and $\text{Cu}(\text{NO}_3)_2$ (**Figure S7**). The precursor maintains a crystalline structure over the whole calcination temperature range (from non-calcined to 800 °C). The diffractogram of $\text{Cu}(\text{ac})_2$ is shown at 25°C and then its decomposition from 100°C to 200°C. At 220°C we see the formation of mixed metallic Cu, Cu_2O and CuO species – known from previous work that acetate decomposes through a radical formation – then by gradually increasing the calcination temperature, all Cu oxidizes to CuO. For $\text{Cu}(\text{NO}_3)_2$ the same trend is observable - yet, without reduction intermediates - where a gradual decomposition of the nitrate salt takes place until all Cu is transformed to CuO. [1,2]

Composites: The XRD analysis further confirmed the exclusive presence of the anatase phase (**Figure S7** and **Table S3**), in line with Raman Spectroscopy. The patterns show no significant peak broadening or peak shift, even for the 400°C treated sample, while only small changes of the crystal parameters upon the thermal treatment can be explained by the relatively small Cu amount present in the samples (~1 at. %). This is in line with recent DFT studies which suggest that a potential Cu incorporation (via interstitial or substitutional Cu:TiO₂ doping) does not result in a pronounced TiO₂ lattice distortion.[3] Both, Raman and XRD results are merely hints for potential interstitial doping of Cu into the TiO₂ lattice at elevated temperatures.

Table S3: Crystal parameters from the $\text{Cu}(\text{ac})_2/\text{TiO}_2$ sample shown in **Figure S7**. Pure anatase vs. non-calcined (RT) and at 400 °C treated $\text{Cu}(\text{ac})_2/\text{TiO}_2$ samples. As a standard reference material was used Si with a certified lattice parameter of 0.543123 ± 0.000008 nm (SRM 604d) at 22.5 °C in order to determine the crystal lattice parameter changes.

	XRD Crystal lattice parameters		
	a	c	Si
TiO ₂ -anatase	3.779	9.491	5.431
Cu/TiO ₂ - RT	3.788	9.510	5.431
Cu/TiO ₂ - 400 °C	3.790	9.509	5.431

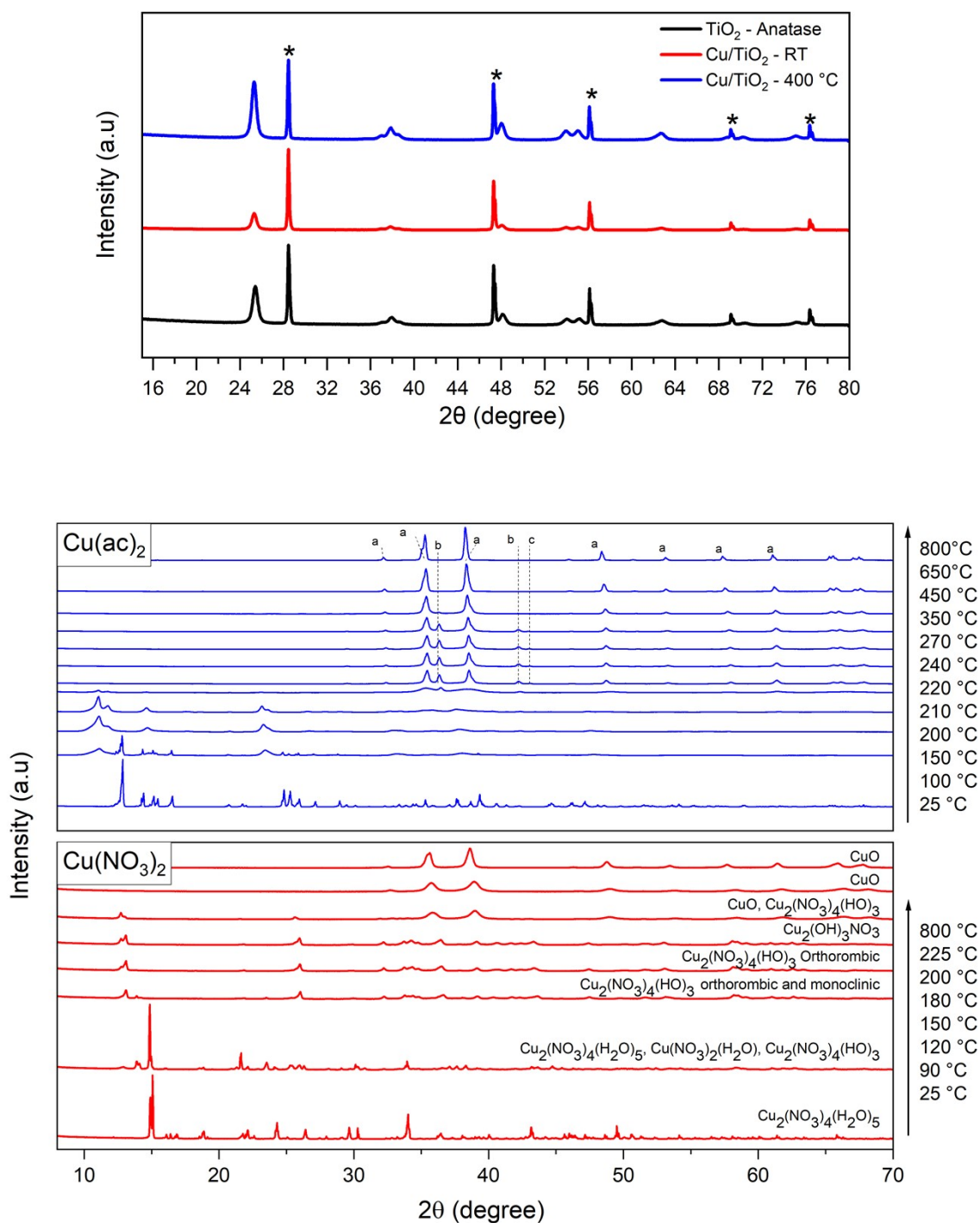


Figure S7: Top: XRD of the non-calcined and 400 °C treated Cu(ac)₂/TiO₂. The (*) indicates the Si phase used as internal standard to determine the crystal lattice parameters changes. All other phases belong to anatase TiO₂. Bottom: in-situ XRD; thermal decomposition evolution of the pure precursors. (a) Cu(ac)₂ and (b) Cu(NO₃)₂.

6. Infrared spectroscopy (FT-IR)

We analyzed for comparison the pure precursors and the composites at different thermal treatments to determine correlations of their behaviors.

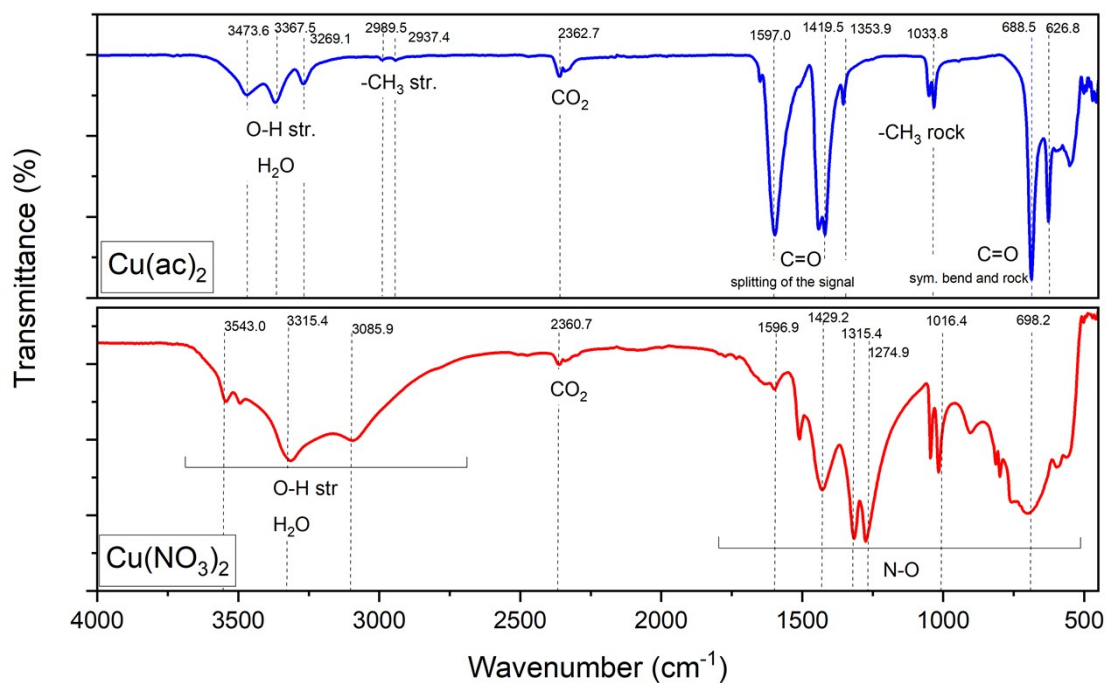


Figure S8: IR-ATR of the pure precursors, $\text{Cu}(\text{ac})_2$ and $\text{Cu}(\text{NO}_3)_2$.

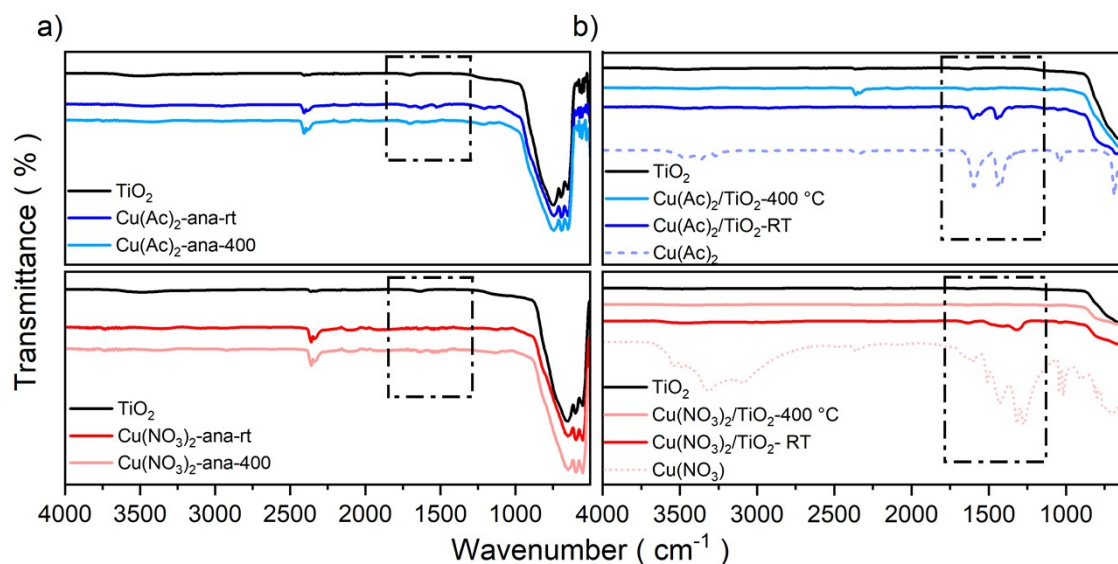


Figure S9: Full range FTIR-ATR of the $\text{Cu}(\text{ac})_2/\text{TiO}_2$ and $\text{Cu}(\text{NO}_3)_2/\text{TiO}_2$ samples at different calcination temperatures. a) 1 at. % of Cu and b) 5 at. % of Cu.

7. XPS

The XPS measurements were done with two different XPS machines, one with a monochromatic Al-K α source and one equipped with a dual anode providing Al-K α and Mg-K α radiation. Furthermore, measurements were done depositing the samples on an indium foil (measured with the mono source) and on a carbon tape (used for the dual anode). The indium foil was used to avoid charging effects and so to determine a correct work function and valence band. The dual anode was used to resolve the Cu-auger bands (Cu LMM), using the Mg-K α radiation, due to an overlap of the Ti 2s signals. By using this radiation, an apparent shift of binding energy of the auger band is induced (see the corresponding surveys).

Surveys:

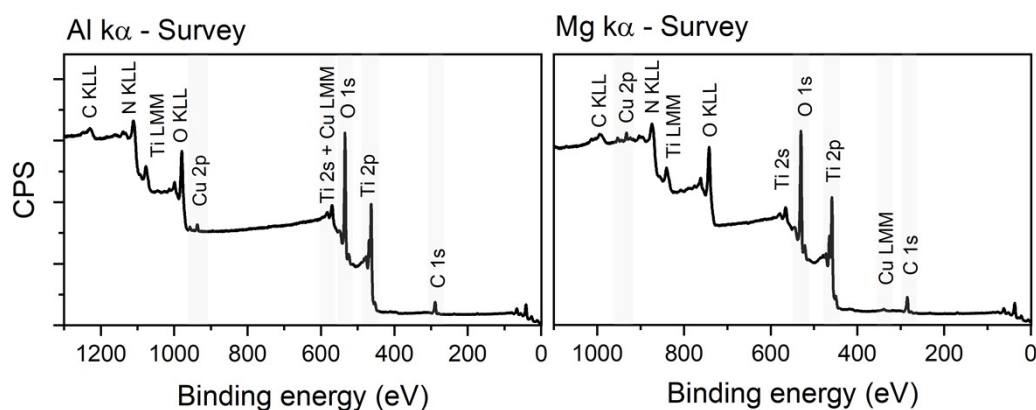


Figure S10: XPS survey spectra of the Cu(NO₃)₂/TiO₂ samples. Left: measured with the Al-K α . Right: measured with the Mg-K α . Note the shift O KLL, Ti LMM and Cu LMM auger signals.

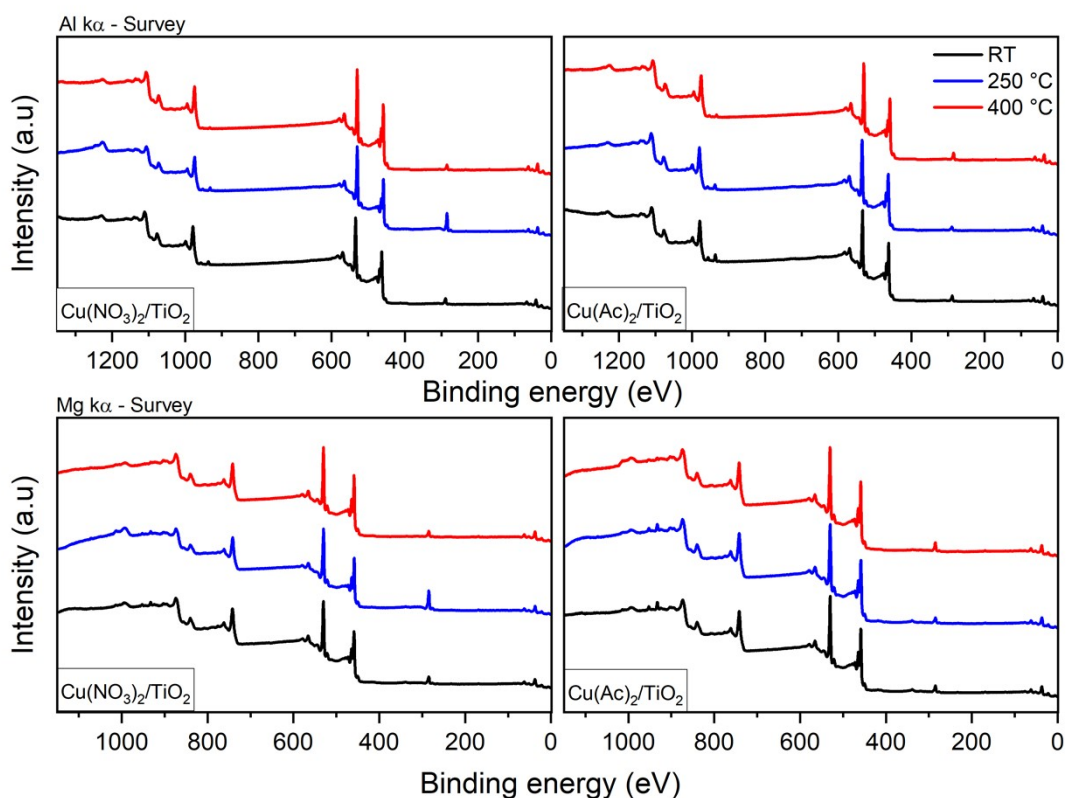


Figure S11: All surveys of the different calcined $\text{Cu}(\text{NO}_3)_2/\text{TiO}_2$ and $\text{Cu}(\text{ac})_2/\text{TiO}_2$ samples. Top: measured with Al-K α . Bottom: measured with Mg-K α .

Table S4: Survey quantifications from the corresponding Al-K α and Mg-K α x-ray source.

	Al-k α				Mg-k α			
	Ti 2p	Cu 2p	C 1s	O 1s	Ti 2p	Cu 2p	C 1s	O 1s
$\text{Cu}(\text{ac})_2/\text{TiO}_2$	at %							
RT	23.4	0.9	18.6	57.4	22.7	1.0	20.5	55.8
250 °C	24.4	0.8	14.3	60.6	23.4	1.0	17.3	58.3
400 °C	23.0	0.3	21.2	55.5	22.2	0.3	23.0	54.5
	Al-k α				Mg-k α			
	Ti 2p	Cu 2p	C 1s	O 1s	Ti 2p	Cu 2p	C 1s	O 1s
$\text{Cu}(\text{NO}_3)_2/\text{TiO}_2$	at %							
RT	22.2	0.6	20.4	56.9	21.3	0.5	23.8	54.4
250 °C	14.5	0.3	42.3	42.9	14.4	0.3	44.0	41.2
400 °C	25.1	0.2	15.4	59.3	24.0	0.2	19.4	56.5

C 1s:

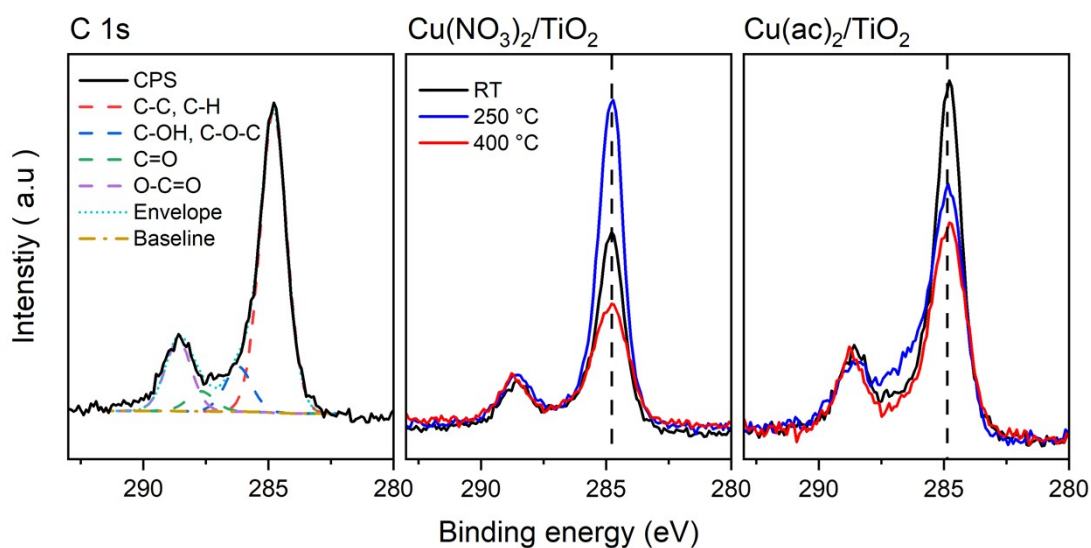


Figure S12: All C 1s of the different calcined $\text{Cu}(\text{NO}_3)_2/\text{TiO}_2$ and $\text{Cu}(\text{ac})_2/\text{TiO}_2$ samples. From left to right: The deconvoluted data of the non-calcined $\text{Cu}(\text{ac})_2/\text{TiO}_2$ with the characteristic adventitious carbon species. All $\text{Cu}(\text{NO}_3)_2/\text{TiO}_2$ and $\text{Cu}(\text{ac})_2/\text{TiO}_2$ C 1s spectra.

O 1s:

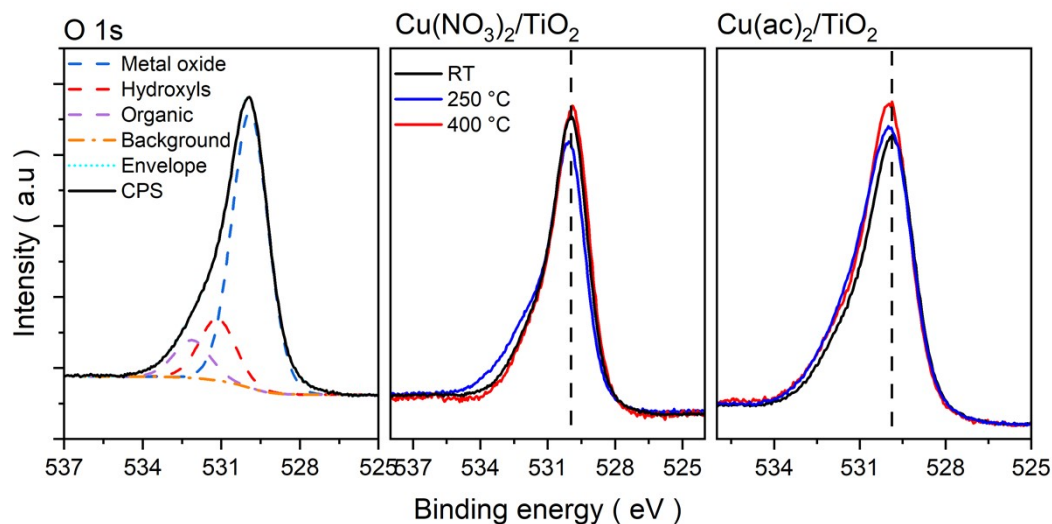


Figure S13: XPS O 1s detail spectra of all different calcined $\text{Cu}(\text{NO}_3)_2/\text{TiO}_2$ and $\text{Cu}(\text{ac})_2/\text{TiO}_2$ samples. Left to right: the deconvoluted data of the non-calcined $\text{Cu}(\text{ac})_2/\text{TiO}_2$ sample. All $\text{Cu}(\text{NO}_3)_2/\text{TiO}_2$ and $\text{Cu}(\text{ac})_2/\text{TiO}_2$ spectra.

8. XPS and XRF

Table S5. XRF vs. XPS (from the surveys and recalculated to set in a ratio to Ti. Ti set to 100) Cu at. % in relation to Ti quantification. Data are shown in **Figure 4** in the manuscript.

	Cu amount in at. %					
	Cu(ac) ₂ /TiO ₂			Cu(NO ₃) ₂ /TiO ₂		
	XPS		XRF	XPS		XRF
	Al-K _α	Mg-K _α		Al-K _α	Mg-K _α	
RT	3.8	4.6	1.08	2.5	2.3	0.69
150 °C	-	-	1.07	2.4	2.6	0.73
250 °C	3.2	4.2	1.05	1.9	2.2	0.67
400 °C	1.3	1.3	0.99	0.9	0.7	0.64

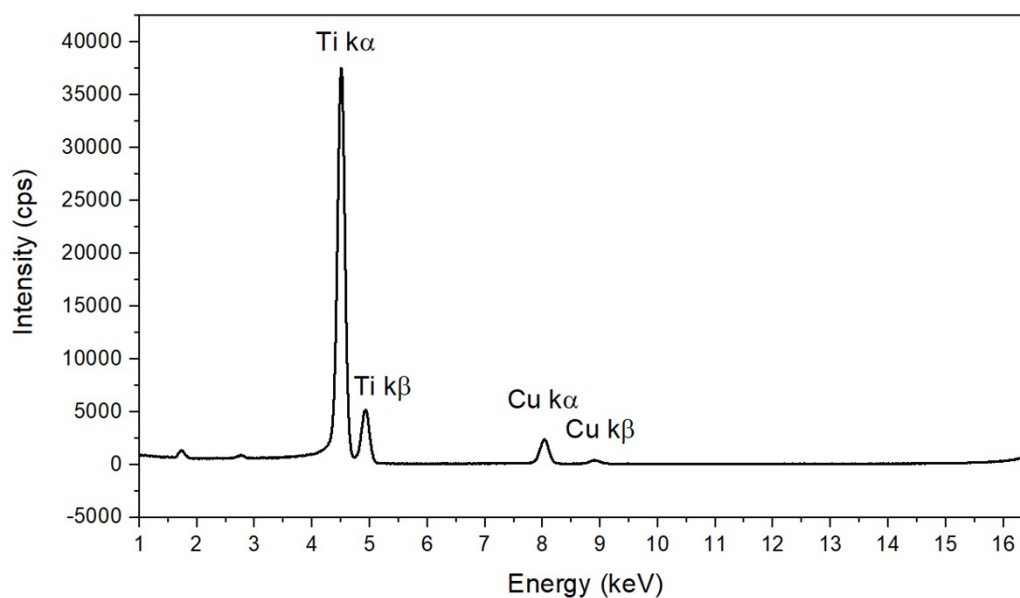


Figure S14: XRF full spectra of one of the analyzed samples, all other samples spectra look the same just with intensity shifts. Corresponding data are shown in **Table S5**. The spectra show the corresponding Ti and Cu peaks without further contribution of other species. The peak at 1.8 keV and 2.9 keV belong to the Si from the detector and Ar from the measuring atmosphere, respectively.

9. DRS, Tauc plots, UPS and VB-XPS

The thermal decomposition of the pure precursors, analyzed by In-situ XRD, see **Figure S7**, show for nitrate that Cu^{2+} stays present for the whole decomposition, while for acetate different oxidation states are generated over thermal treatment until getting fully oxidized to Cu^{2+} again. By analyzing the DRS profiles, we see these changes represented in the absorption range from 500 to 900 nm corresponding to Cu^{2+} .

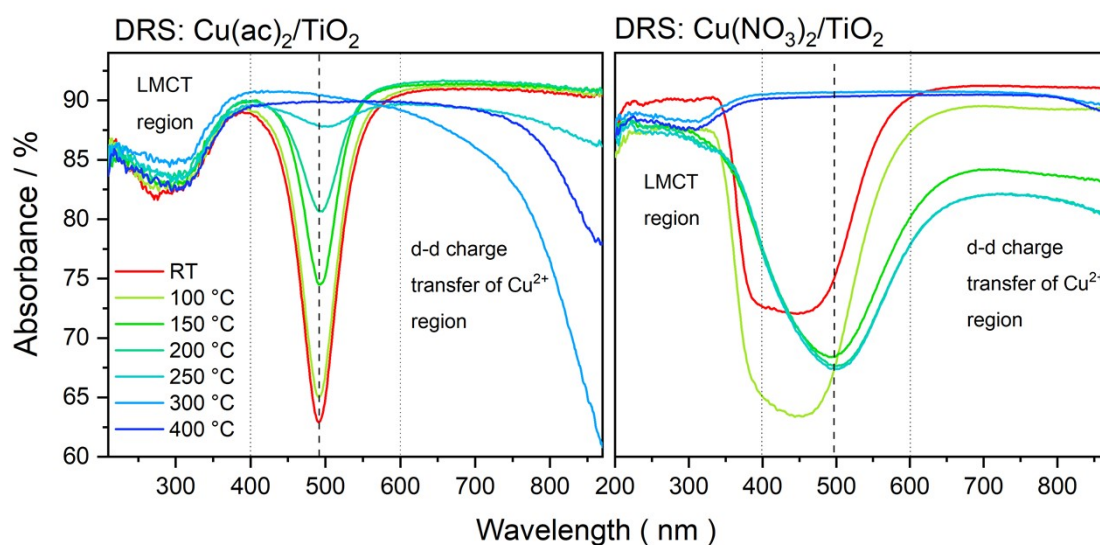


Figure S15. DRS of the pure precursors (a) $\text{Cu}(\text{NO}_3)_2$ and (b) $\text{Cu}(\text{ac})_2$ at different thermal treatments, showing the evolution of the DRS profile by decomposition of the nitrate and acetate ligand and the formation of the different Cu oxides.

The band gap, work function and valence band maximum were determined with a linear fit interpolated to the zero Tauc function and zero Intensity, respectively. The corresponding errors are from the linear fit where 6 different points were taken, and the average was taken as the corresponding value.

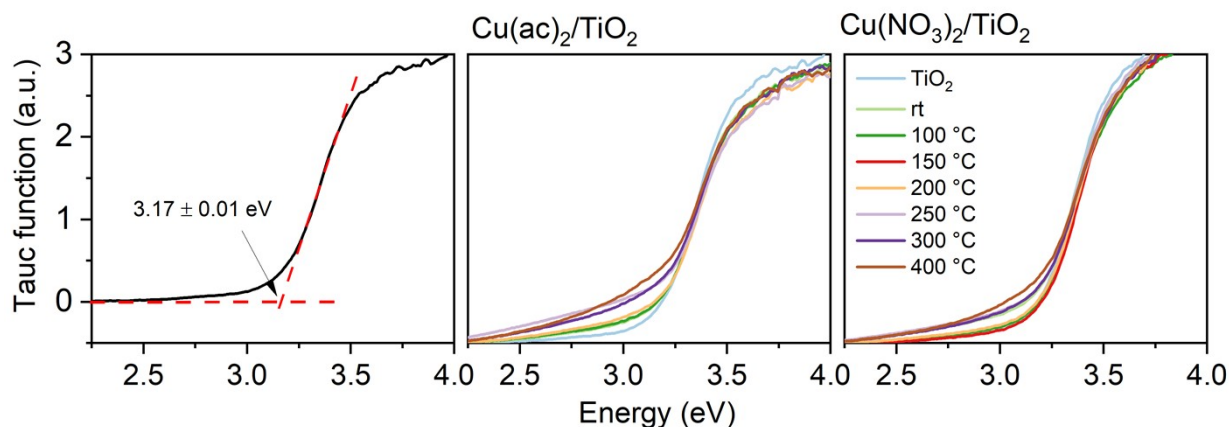


Figure S16. DRS Tauc plots. (a) representation of how the band gaps were taken by extrapolation to the zero Tauc function. (b) Tauc plots of $\text{Cu}(\text{NO}_3)_2/\text{TiO}_2$ and (c) $\text{Cu}(\text{ac})_2/\text{TiO}_2$ at different thermal treatments.

Table S6. DRS Tauc plot band gap values table obtained from **Figure S16**.

	$\text{Cu}(\text{ac})_2/\text{TiO}_2$	$\text{Cu}(\text{NO}_3)_2/\text{TiO}_2$
	E_g - Band gap	E_g - Band gap
	eV	eV
TiO_2	3.17	3.17
RT	3.12	3.13
100 °C	3.11	3.13
150 °C	3.11	3.13
200 °C	3.09	3.12
250 °C	3.06	3.11
300 °C	3.05	3.10
400 °C	3.00	3.07

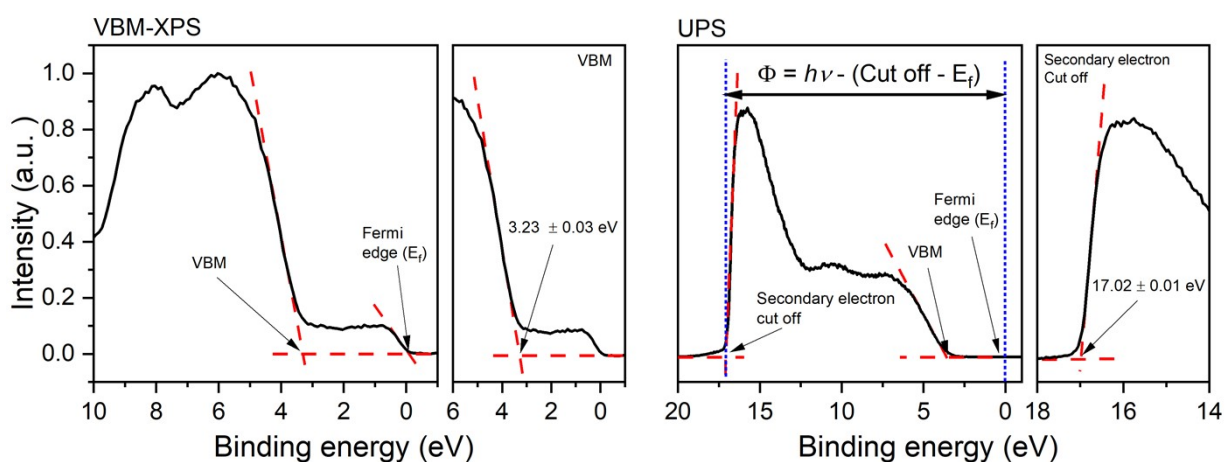


Figure S17. a) VB-XPS and b) UPS to determine the valence band maximum and work function, respectively. Representation of how the values were taken for all samples, here only shown TiO_2 . $h\nu = 21.2$ eV (He-II source) and $E_f = 0$ eV.

Table S7. Data used in **Figure 5h** from the main manuscript. (*) Data calculated from VB-XPS, Work function and E_g by taking the vacuum energy ($E_{vac} = 0$ eV) as the reference. The former values were obtained from the corresponding VB-XPS, UPS and DRS spectra where the fermi edge is the reference ($E_f = 0$ eV). All data in eV.

	Cu(ac) ₂ /TiO ₂						Cu(NO ₃) ₂ /TiO ₂					
	VB-XPS	Work function	E_g	Fermi level*	VBM*	CB*	VB-XPS	Work function	E_g	Fermi level*	VBM*	CB*
TiO ₂	3.2	4.2	3.2	-4.2	-7.4	-4.2	3.2	4.2	3.2	-4.2	-7.5	-4.3
RT	3.0	4.2	3.1	-4.2	-7.2	-4.1	3.0	3.9	3.1	-3.8	-6.9	-3.8
250 °C	3.0	4.0	3.2	-4.0	-7.0	-4.0	3.0	4.4	3.1	-4.3	-7.3	-4.2
400 °C	3.1	4.1	3.0	-4.1	-7.2	-4.2	3.3	4.2	3.1	-4.1	-7.4	-4.3

10. DRS and XRF before and after washing of Cu(NO₃)₂/TiO₂

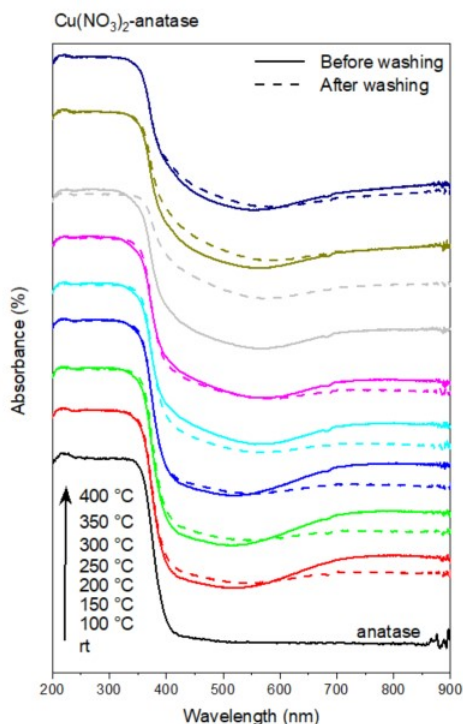


Figure S18: DRS of the Cu(NO₃)₂/TiO₂ before and after washing.

Table S8: XRF measurements of the Washing experiment. Cu at. % of the samples before and after washing (Ti is set to 100) and the corresponding decrease of Cu % used in **Figure 6** in the manuscript.

	Cu(ac) ₂ /TiO ₂			Cu(NO ₃) ₂ /TiO ₂		
	Cu concentration in at. %		Decrease after washing %	Cu concentration in at. %		Decrease after washing %
	Before washing	After washing		Before washing	After washing	
RT	1.19	0.45	62.52	0.96	0.13	86.26
100°C	1.54	0.47	69.29	1.08	0.12	88.73
150°C	1.21	0.46	61.78	0.93	0.12	87.42
200°C	1.17	0.49	58.34	0.85	0.17	80.48
250°C	1.18	0.48	59.23	0.81	0.25	68.67
300°C	1.13	0.58	49.02	0.75	0.41	46.03
350°C	1.01	0.85	15.96	0.70	0.58	17.23
400°C	1.02	0.89	12.41	0.76	0.63	17.88

11. Cu amount effect on the HER activity

To determine the dependency of the amount of at. Cu % versus HER we prepared a model system by using the photodeposition method. This method consists of preparing a Cu solution with the suspended TiO₂-anatase nanoparticles. Then by UV-light illumination of the system, an excited electron is generated that reacts with the Cu in solution (electron transfer from TiO₂ to Cu, inducing the reduction of Cu). In parallel, it is in-situ detected the amount of Hydrogen that is generated by this photodeposition. In this method, the HER rate is directly dependent on the Cu amount available in the solution able to deposit on TiO₂ (see **Figure 19**). The difference in this method to the wet impregnation is when the HER rate is analyzed under light illumination Cu deposits from the solution on TiO₂ (photodeposition) while in the wet impregnation Cu is already on the TiO₂ surface. Thus, if a Cu redox shuttle takes place, in the first case it goes from solution on TiO₂, in the second it goes from the TiO₂ surface in solution and back. Thus, to further investigate the dependence of HER on the surface availability of Cu, we prepared Cu/TiO₂ photocatalysts with different at. % of Cu on TiO₂ surface – ranging from 0.01 to 1 at. % – using the photo-deposition method (see **Figure S19b**). The reasoning is: in the photodeposition process – TiO₂ is suspended in the HER solution with solubilized Cu - Cu can undergo redox shuttling with the TiO₂ surface. In our systems, prepared by wet impregnation, TiO₂ is impregnated previously with Cu, hence, Cu must go from the TiO₂ surface into the solution to carry out the HER reaction. Thus, if Cu diffuses into the TiO₂ lattice, and is consequently less accessible to the solution to undergo redox shuttling a decreased activity would be expected. In **Figure S19b** we see, for the photodeposition model, that a decreasing amount of Cu available leads to reduced activity. In **Figure 1** (from the main manuscript) we saw a gradual decrease of HER rate by increasing temperature until reaching 72 % of the peak performance at 400 °C, corresponding to HER rate of 14.81 μmol h⁻¹ for Cu(ac)₂/TiO₂ (**Table S9**). Correlating these data with the photodeposition model study (**Figure S19b**), we see that this corresponds to a Cu at. % less than 0.1 %. The XPS survey quantification further showed that 0.3 and 0.2 at.% for the 400 °C Cu(ac)₂/TiO₂ and Cu(NO₃)₂/TiO₂, respectively, is still present on the TiO₂ surface.

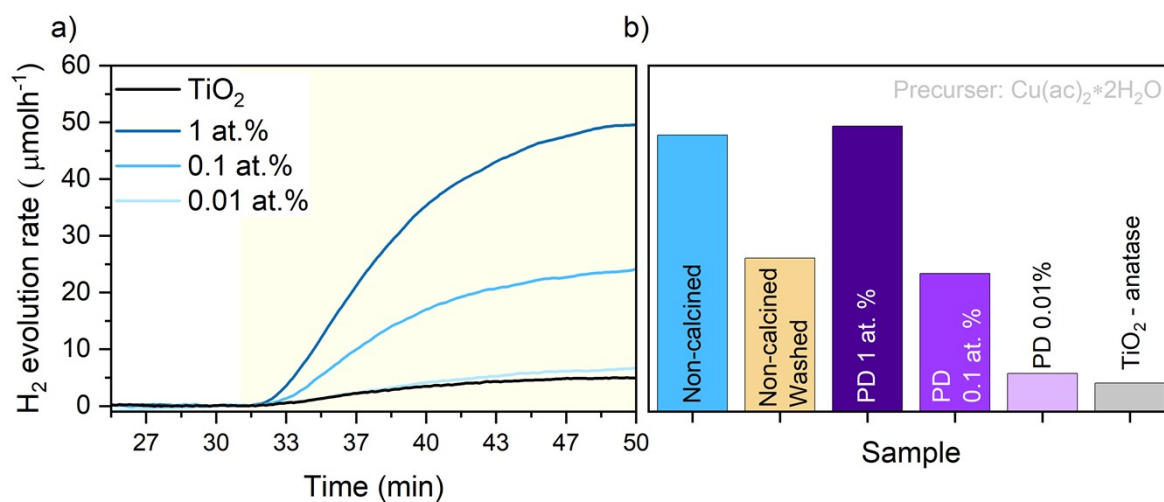


Figure S19. a) HER dependency with different Cu at. % photodeposited on TiO₂. Ranging from 0.01 to 1 at. % of photo-deposited Cu. b) Bar diagram showing the absolute HER values for the photodeposited (PD) samples and the non-calcined before and after washing, as well as the reference TiO₂.

Table S9: Photodeposition (PD) experiment: HER rate maximum after 20 minutes of illumination. Values are taken from the graphs **Figure S19**.

Cu at %	H ₂ evolution rate μmol h ⁻¹
TiO ₂ -Anatase	4.97
Non-calcined	47.97
Non-calcined Washed	26.63
PD 1%	49.54
PD 0.1%	23.97
PD 0.01%	6.65

12. DFT calculations

Perfect anatase TiO₂ surface

Figure S20 shows that the anatase TiO₂ (101) surface has a stepped structure. Threefold coordinated O atoms (O_{3c}) and sixfold coordinated Ti atoms (Ti_{6c}) are fully saturated and have bulk coordination whereas the twofold (O_{2c}) and fivefold (Ti_{5c}) atoms are undercoordinated. The O_{2c} atoms are located at the ridges of the saw-tooth-like structure, and after optimization, they relax inwards by ~ 0.16 Å with respect to bulk TiO₂. The three-fold coordinated O_{3c} atoms relax outwards by ~ 0.07 Å, while the Ti_{5c} and Ti_{6c} atoms relax inwards by ~ 0.15 Å and ~ 0.16 Å respectively, so that the surface exhibits a slightly buckled structure.

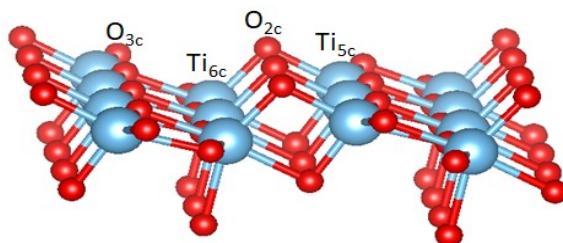


Figure S20: Side view of the top-most layer of the anatase TiO₂ (101) surface (in the 1 x 3 supercell). Red and blue spheres corresponded to O and Ti atoms respectively.

Table S10: Shortest Cu-O bonds between a Cu Atom (of the pure Cu clusters adsorbed on the anatase TiO₂ (101) surface) and O atoms (O_{2c} and O_{3c}) of TiO₂. Cu₅ (1) and Cu₅ (2) refer to chain-like and 3D-like structures, respectively. The results for different Cu atoms are separated by semicolons. “(2)” means two bonds of same length and (*) indicates a Cu in the subsurface.

Compound	Cu-O _{2c} (Å)	Cu-O _{3c} (Å)
TiO ₂ -Cu	1.87(2)	2.33;2.47
TiO ₂ -Cu*	1.96(2)*	2.03;2.17*
TiO ₂ -Cu ₂	(1.88,1.89);(1.88,1.89)	(2.34,2.52);(2.34,2.52)
TiO ₂ -Cu ₃	1.90(2);1.90(2);1.90(2)	(2.28,2.46);(2.29,2.46);(2.28,2.46)
TiO ₂ -Cu ₅ (1)	1.97;2.11;(2.09,2.10);(2.04,2.15);2.83	(2.81,2.71);(2.30,2.31);2.30;2.42;-
TiO ₂ -Cu ₅ * (1)	1.99;2.02;1.87(2);1.87(2);(2.23,2.24)*	(2.42,2.80);2.31;(2.41,2.53);(2.42,2.53);1.99(2)*
TiO ₂ -Cu ₅ (2)	1.86;-;-;2.94;1.89	-;-;2.00;2.75

Table S11: Adsorption energy (eVatom⁻¹) and Bader charge for Cu_x (x=1, 2, 3, 5) clusters adsorbed on the anatase TiO₂ (101) surface. Cu₅ (1) and Cu₅ (2) refer to chain-like and 3D-like structures, respectively. For comparison, the cohesive energy for bulk CuO is 2.75 eV. (*) indicates a Cu in the subsurface. E_{ads} in the subsurface is the equivalent of the binding energy. Bader charges <0.4 correspond to Cu⁰, 0.4 – 0.7 to Cu⁺ and >0.7 to Cu⁺².

Compound	E _{ads} (eV atom ⁻¹)	Bader charge (e ⁻)
TiO ₂ -Cu	2.24	0.68
TiO ₂ -Cu*	1.90*	0.69*
TiO ₂ -Cu ₂	2.08	0.68,0.68
TiO ₂ -Cu ₃	1.99	0.68,0.68,0.68
TiO ₂ -Cu ₅ (1)	1.9	0.15,0.13,0.48,0.41,-0.06
TiO ₂ -Cu ₅ * (1)	1.84	0.17,0.17,0.66,0.66,0.71*
TiO ₂ -Cu ₅ (2)	2.26	0.33,0.07,-0.12,0.17,0.34

References

- [1] J. S. Schubert, J. Popovic, G. M. Haselmann, S. P. Nandan, J. Wang, A. Giesriegl, A. S. Cherevan, D. Eder, *Journal of Materials Chemistry A* 2019, 7, 18568.
- [2] Z. Lin, D. Han, S. Li, *J Therm Anal Calorim* 2012, 107, 471.
- [3] A. M. Alotaibi, B. A. D. Williamson, S. Sathasivam, A. Kafizas, M. Alqahtani, C. Sotelo-Vazquez, J. Buckeridge, J. Wu, S. P. Nair, D. O. Scanlon, I. P. Parkin, *ACS Appl. Mater. Interfaces* 2020, DOI 10.1021/acsami.9b22056.